Turbulence Phase Space in Simple Magnetized Toroidal Plasmas

Paolo Ricci[1,*] and B. N. Rogers[2,†]

[1]Centre de Recherches en Physique des Plasmas - École Polytechnique Fédérale de Lausanne, Association EURATOM-Confédération Suisse, CH-1015 Lausanne, Switzerland

[2]Department of Physics and Astronomy, Dartmouth College, Hanover, New Hampshire 03755, USA

(Received 4 December 2009; published 7 April 2010)

Plasma turbulence in a simple magnetized torus (SMT) is explored for the first time with three-dimensional global fluid simulations. Three turbulence regimes are described: an ideal interchange mode regime, a previously undiscovered resistive interchange mode regime, and a drift-wave regime. As the pitch of the field lines is decreased, the simulations exhibit a transition from the first regime to the second, while the third—the drift-wave regime—is likely accessible to the experiments only at very low collisionalities.

DOI: 10.1103/PhysRevLett.104.145001 PACS numbers: 52.35.Ra, 52.35.Kt, 52.65.Kj

Simple magnetized torus (SMT) experiments confine a toroidal plasma with a helical magnetic field [1–3]. This configuration has been of long-standing interest to the plasma turbulence and fusion communities for two main reasons. First, it offers a simple and well-diagnosed testbed in which to study the basic physics of plasma turbulence and the associated transport of heat and particles. Second, by virtue of its dimensionless parameters and magnetic geometry, it provides a simplified setting in which to explore one of the most currently important topics in fusion research: the physics of turbulent transport in the edge region of magnetically confined fusion devices such as tokamaks. This topic is important because particles and heat transport across the edge region of these machines largely governs the fusion power output of the entire device [4]. Perhaps more than any other issue, persisting uncertainties related to edge transport continue to undermine our ability to reliably predict the performance of future fusion reactors such as ITER [5].

We present here, based on first-time global three-dimensional fluid simulations of the SMT configuration, a new theoretical understanding of turbulence in the SMT. Our results call for a significant reinterpretation of SMT observations and how they relate to magnetically confined fusion devices. At the relatively high collsionalities typical of the TORPEX experiment [2], the simulations reveal three regimes of turbulence, each driven mainly by a distinct plasma instability: an ideal interchange mode regime, a previously undiscovered resistive interchange mode regime, and a drift-wave (DW) regime. The DW regime, previously assumed to dominate the SMT plasmas as the pitch of the field lines is decreased [6] and long regarded as important to the fusion-relevancy of the SMT concept [7], is in fact found here to be accessible to the experiments only at very low collisionalities. Rather, we find the low pitch regime in TORPEX is dominated by resistive interchange modes, the existence of which in the SMT, due to the global nature of our simulations, is recognized here for the first time. As discussed later, resistive interchange modes are very similar to resistive ballooning instabilities, which are believed to control plasma transport in the far edge (the ''scape off layer'' or SOL) of tokamaks and similar devices [8]. Since the magnetic geometry and parallel boundary conditions of tokamaks and SMTs are also most similar in this far-edge region, we believe our new findings preserve, if not enhance, the fusion relevancy of SMTs.

The most obvious difference between ideal interchange turbulence and turbulence driven by either resistive interchange or DW instabilities is the wave number along the magnetic field: $k_\parallel = 0$ in the former case, while $k_\parallel \neq 0$ in the latter. Considering, for example, the observations of SMT turbulence in the TORPEX device [2], the transition from $k_\parallel = 0$ ideal interchange mode dominated turbulence to a finite $k_\parallel \neq 0$ state is clearly observed as the pitch of the field lines is decreased [6]. The pitch can be expressed in terms of $N = L_v B_\varphi/(2\pi R B_v)$, the total number of field line turns from the bottom of the SMT to the top, where R and L_v are the vessel major radius and height, B_v and B_φ are the vertical and toroidal components of the magnetic field. The pitch decreases as N is increased, and the onset of $k_\parallel \neq 0$ fluctuations is observed for sufficiently large N. In Fig. 1, the vertical mode number l (corresponding to a vertical wave number $k_v = 2\pi l/L_v$) is plotted as a function of N. The $k_\parallel = 0$ regime, in which $l = N$, is observed for small $N \lesssim 7$. The dominant toroidal mode number in this case is $n = 1$—the expected value given $k_\parallel = 0$ and

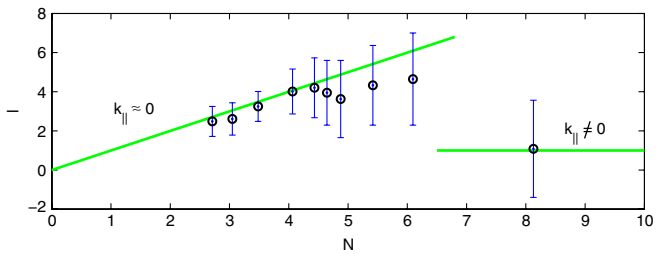

FIG. 1 (color online). l for the turbulence described in Refs. [6].

$l = N$, as we show later. For $N \gtrsim 7$ the turbulence transitions to a state dominated by $l = 1$ fluctuations (one wavelength in the vertical direction from bottom to top), which corresponds to a small but finite $k_\parallel \simeq 1/(RN)$. The dominant toroidal mode number in this regime is $n = 0$—that is, the turbulence becomes toroidally symmetric.

These TORPEX observations are in agreement with our findings, which indicate the presence of (i) an ideal interchange regime characterized by $k_\parallel = 0$, $l = N$, and $n = 1$, (ii) a resistive interchange regime with $k_\parallel \neq 0$, $n = 0$, and $l = 1$, and (iii) a DW regime that is obtained for sufficiently steep gradients $L_p < L_{p,\mathrm{crit}}$ and is characterized by very short vertical wavelengths, $k_\perp \rho_s \sim 0.5$. At the relatively high collisionalities of the TORPEX experiments, however, our simulations suggest the transport driven by interchange modes prevents the gradient scale lengths from ever steepening into the DW dominated regime. This situation is similar to that observed in the far-edge region of tokamaks [8], in which resistive interchange (ballooning) modes rather than DW dominate the transport even in the most weakly collisional cases (H modes). The behavior of l in Fig. 1 therefore reflects a transition from ideal to resistive interchange turbulence.

Resistive interchange modes in the SMT are similar to resistive ballooning modes in the edge region of tokamaks: they have maximum growth rates comparable to the ideal interchange mode $\gamma^2 \sim c_s^2/(RL_p)$ and occur when the conductivity is sufficiently small. The instability threshold follows from the vorticity equation [Eq. (2)]: the polarization drift term $\partial_t \nabla_\perp^2 \phi$ must exceed the line bending term proportional to $\nabla_\parallel j_\parallel$; with Ohm's law [Eq. (5)], $j_\parallel \sim -\sigma_\parallel \nabla_\parallel \phi$, this condition yields $\gamma k_\perp^2 > 4\pi V_A^2 k_\parallel^2 \sigma_\parallel / c^2$. Because $k_\parallel = 1/(NR)$, line bending becomes negligible for sufficiently high N—the reason resistive interchange modes are limited to higher N. Since $k_\perp \sim 2\pi/L_v$ ($l = 1$), the numerical study of such modes requires global simulations that cover the entire SMT domain like those described here. This explains why resistive interchange mode turbulence was overlooked in all previous, nonglobal simulation studies of the SMT (e.g., [9,10]), which were restricted to flux-tubes of vertical extent L_v/N. Although the simulations reported here agree with these earlier works in the low N ideal interchange regime, at higher N the absence of resistive interchange modes in the flux-tube based work led to artificially low transport and turbulence levels. Further discussion of this issue is given below.

Following the TORPEX parameters, we use the drift-reduced Braginskii equations [11] with $T_i \ll T_e$ and $\beta \ll 1$:

$$\frac{\partial n}{\partial t} = \frac{c}{B}[\phi, n] + \frac{2c}{eRB}\left(\frac{\partial p_e}{\partial y} - en\frac{\partial \phi}{\partial y}\right) - \frac{\partial (nV_{\parallel e})}{\partial z} + S_n, \quad (1)$$

$$\frac{\partial \nabla_\perp^2 \phi}{\partial t} = \frac{c}{B}[\phi, \nabla_\perp^2 \phi] - V_{\parallel i}\frac{\partial \nabla_\perp^2 \phi}{\partial z} + \frac{2B}{cm_i Rn}\frac{\partial p_e}{\partial y} + \frac{m_i \Omega_{ci}^2}{e^2 n}\frac{\partial j_\parallel}{\partial z}, \quad (2)$$

$$\frac{\partial T_e}{\partial t} = \frac{c}{B}[\phi, T_e] + \frac{4c}{3eRB}\left(\frac{7}{2}T_e\frac{\partial T_e}{\partial y} + \frac{T_e^2}{n}\frac{\partial n}{\partial y} - T_e\frac{\partial \phi}{\partial y}\right) + \frac{2}{3}\frac{T_e}{en}0.71\frac{\partial j_\parallel}{\partial z} - \frac{2}{3}T_e\frac{\partial V_{\parallel e}}{\partial z} - V_{\parallel e}\frac{\partial T_e}{\partial z} + S_T, \quad (3)$$

$$\frac{\partial V_{\parallel i}}{\partial t} = \frac{c}{B}[\phi, V_{\parallel i}] - V_{\parallel i}\frac{\partial V_{\parallel i}}{\partial z} - \frac{1}{nm_i}\frac{\partial p_e}{\partial z}, \quad (4)$$

$$m_e n\frac{\partial V_{\parallel e}}{\partial t} = m_e n\frac{c}{B}[\phi, V_{\parallel e}] - m_e n V_{\parallel e}\frac{\partial V_{\parallel e}}{\partial z} - T_e\frac{\partial n}{\partial z} + en\frac{\partial \phi}{\partial z} - 1.71n\frac{\partial T_e}{\partial z} + \frac{en}{\sigma_\parallel}j_\parallel, \quad (5)$$

where $p_e = nT_e$, $[a, b] = \partial_x a \partial_y b - \partial_y a \partial_x b$, $j_\parallel = en(V_{\parallel i} - V_{\parallel e})$, $\Omega_{ci} = eB/(m_i c)$, and S_n and S_T are the density and temperature sources. The x coordinate denotes the radial direction, z is parallel to B, and y is the direction perpendicular to x and z (for $B_v \ll B_\varphi$ the vertical and y directions are approximately the same).

We solve Eqs. (1)–(5) on a field-aligned grid using a finite difference scheme with Runge-Kutta time stepping and small numerical diffusion terms. The computational domain has an annular shape with a cross section $x = 0$ to $x = L_x$ and $y = 0$ to $y = L_y$. At $x = 0$ and $x = L_x$, Dirichelet boundary conditions are used for n, T_e, ϕ, and $\nabla_\perp^2 \phi$ and Neuman boundary conditions for $V_{\parallel e}$ and $V_{\parallel i}$. At $y = 0$ and $y = L_y$, for the parallel velocities we use Bohm boundary conditions $V_{\parallel i} = \pm c_s$ and $V_{\parallel e} = \pm c_s \exp(\Lambda - e\phi/T_e)$, with $\Lambda = \log\sqrt{m_i/(2\pi m_e)}$; at the same location, we have explored both Dirichelet and Robin boundary conditions for n and T_e, and for ϕ we use both $e\phi = \Lambda T_e$ (implying $V_{\parallel e} = V_{\parallel i}$) and a boundary condition of the form $\partial_y \phi \propto (e\phi - \Lambda T_e)$, all with similar results for the parameters explored here. The profiles of S_n and S_T mimic the EC and UH resonance layer in TORPEX, and are assumed to have the form $S_{\mathrm{EC}} \exp[-(x - x_{\mathrm{EC}})^2/\lambda_{\mathrm{EC}}^2] + S_{\mathrm{UH}} \exp[-(x - x_{\mathrm{UH}})^2/\lambda_{\mathrm{UH}}^2]$ [12]. The parameters used in the simulations are $S_{\mathrm{UH}}/S_{\mathrm{EC}} = 1.5$, $\lambda_{\mathrm{UH}} = 5\rho_s$, $\lambda_{\mathrm{EC}} = 2.5\rho_s$, $x_{\mathrm{UH}} = 35\rho_s$, $x_{\mathrm{EC}} = 15\rho_s$, $m_i/m_e = 200$, $\Lambda = 3$, $R = 200\rho_s$, $L_x = 100\rho_s$, and $L_y = 64\rho_s$.

The n and T_e profiles steepen due to the sources until turbulence is triggered, leading to transport from the source region to the low-field side. The typical character of the turbulence observed for low N and low plasma resistivity $\nu = e^2 n/(m_i \sigma_\parallel)$ is shown in Fig. 2. The turbulence is driven by the ideal interchange mode with $k_\parallel = 0$ and a vertical wavelength determined by the return of the field line in the poloidal plane, $k_y = 2\pi N/L_v$. The vertical mode number satisfies $l = N$ and the toroidal cut shows a toroidal mode number $n = 1$. The consistency of $n = 1$, $k_\parallel = 0$, and $l = N$ follows from $k_\parallel = \mathbf{k} \cdot \mathbf{b} = k_v B_v/B + k_\varphi B_\varphi/B$. Given $B_v/B_\varphi = L_v/(2\pi RN)$, $k_\parallel$ may be written in terms of the vertical mode number l ($k_v = 2\pi l/L_v$), the toroidal mode number n ($k_\varphi = -n/R$), and the parallel mode number m [$k_\parallel = m/(NR)$] as $m/(NR) = (B_\varphi/B) \times [l/(NR) - n/R]$ or, assuming $B_\varphi \simeq B$ for small B_v, as $m \simeq l - nN$. The dominance of $k_\parallel = 0$ fluctuations at low N is

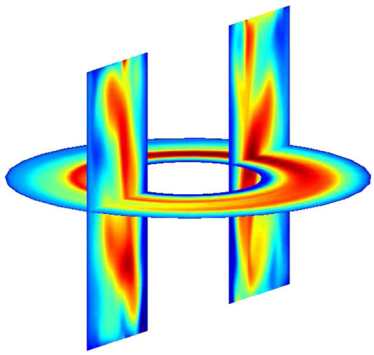

FIG. 2 (color online). Snapshot of ϕ in two poloidal cross sections and in a toroidal plane for $N = 2$, $\nu = 0.01 c_s/R$.

consistent with experimental observations in TORPEX [6], Helimak [13], and BLAAMAN [3], and has been previously explored with numerical simulations in two-dimensions [10]. When N or ν are increased, however, the turbulence enters a new regime shown in Fig. 3, in which the dominant mode is toroidally symmetric ($n = 0$), $k_\parallel \neq 0$, and the typical vertical wavelengths are comparable to the height of the machine, $k_y = 2\pi/L_v$ ($l = 1$). The character of these simulations agree with the high N TORPEX experimental observations in Fig. 1.

The linear stability analysis of Eqs. (1)–(5) provides an explanation of these results. In Fig. 4 we show the vertical mode number l of the fastest growing instability, maximized over all possible values of $l = \pm 1, \pm 2, \ldots$ and $n = 0, \pm 1, \pm 2, \ldots$ (and $m = l - nN$). We consider $\eta = L_n/L_T \simeq 1$. Indicative TORPEX parameters are represented by the center plot of Fig 4: $\nu \sim 0.1 c_s/R$, $L_v \sim 64\rho_s$, and $L_n/R \simeq 0.14$. Consistent with both our numerical simulations and the experimental results, when $N \gtrsim 10$ the dominant instability in the system makes a transition from $l = N$ to $l = 1$.

At least four instabilities are present in the linear dispersion relation. The ideal interchange mode has a flutelike character with $k_\parallel = 0$, i.e. $m = 0$. Since $m \simeq l - nN = 0$, the vertical and toroidal mode numbers l and n are related by $l = nN$. In the $k_\parallel = 0$ limit the linear dispersion relation of Eqs. (1)–(5) becomes $(b_0 + b_1\gamma + b_2\gamma^2 + b_3\gamma^3) = 0$, with $b_0 = 20i\omega_d^2(2\omega_d - \omega_*)/3$, $b_1 = 20(k_y^2\rho_s^2 - 1)\omega_d^2/3 + 2(\eta + 1)\omega_*\omega_d$, $b_2 = 20i\omega_d k_y^2\rho_s^2/3$, $b_3 = -k_y^2\rho_s^2$, $\omega_d = k_y\rho_s c_s/R$, and $\omega_* = k_y\rho_s c_s/L_n$. The peak growth rate occurs for $k_y \to 0$, and is given by $\gamma = \gamma_I$ with $\gamma_I = c_s[2/(RL_p) - 20/(3R^2)]^{1/2}$. (The stabilizing contribution comes from curvature-driven plasma compressibility terms in Eqs. (1) and (3), typically small in the tokamak edge where $L_p \ll R$). Stabilizing contributions associated with finite $k_y\rho_s$ become important for $k_y\rho_s \gtrsim 0.3R\gamma_I/c_s$. The fastest growing mode is thus achieved at the smallest allowed value of $k_y \simeq 2\pi l/L_v$, which given $l = nN$ is $l = N$ for toroidal mode number $n = 1$, i.e. $k_y = 2\pi N/L_v$. With this k_y, the $k_y\rho_s$ condition $k_y\rho_s \gtrsim 0.3R\gamma_I/c_s$ can be written as $\alpha_\perp \gtrsim 1$ where $\alpha_\perp = 2\pi N\rho_s c_s/(0.3L_v R\gamma_I)$. The condition $\alpha_\perp = 1$ is represented by the white lines in Fig. 4; the regions near and below these curves, $\alpha_\perp \lesssim 1$, are thus favorable for ideal interchange modes with $l = N$. Figure 2 reflects the typical character of the ideal interchange regime.

The second instability present in the system is the resistive or electron inertia-driven interchange mode. We consider the limit $\gamma_I \gg k_\parallel c_s$ in which sound wave coupling may be neglected, and $k_y\rho_s < 0.3R\gamma_I/c_s$, which is typically well satisfied for the low $k_y \sim 2\pi/L_v$ values of interest in this case. The linear dispersion relation thus reduces to $\gamma^2 = \gamma_I^2 - \gamma k_\parallel^2 c_s^2/(k_y^2\rho_s^2\hat{\nu})$, $\hat{\nu} = \nu + \gamma m_e/m_i$. The peak growth rate occurs for $k_\parallel \to 0$ and is $\gamma = \gamma_I$. For finite $k_\parallel$, γ decreases with $k_\parallel$ until stability is reached for $k_\parallel^2 c_s^2 \sim 2k_y^2\rho_s^2\gamma_I\hat{\nu}$. Given $m \simeq l - nN$, the longest nonzero parallel wavelength, $m = 1$, is achieved for $n = 0$ and $l = 1$. Although the growth rate of this mode is reduced by finite $k_\parallel$ effects below the maximal value of $\gamma = \gamma_I$ at

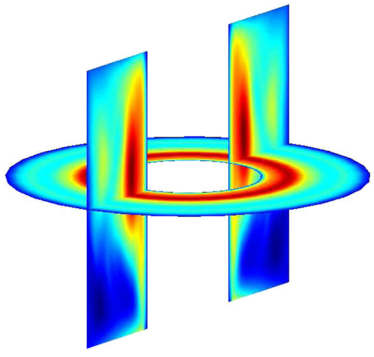

FIG. 3 (color online). As in Fig. 2, for $N = 16$, $\nu = 1 c_s/R$.

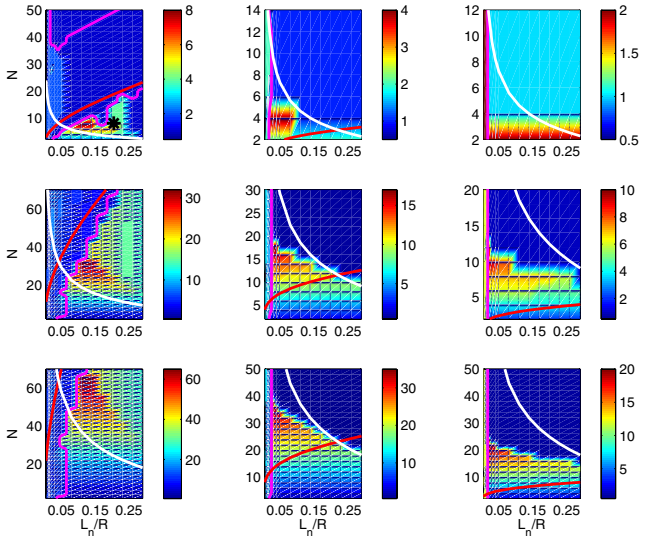

FIG. 4 (color online). Phase space diagram for $L_v = 16$, 64, $128\rho_s$ (top, center, bottom); $\nu = 0.0001$, 0.1, $1 c_s/R$ (left, center, right). $m_i/m_e = 1836$. The red line denotes $\alpha_\parallel = 1$, white is $\alpha_\perp = 1$, magenta is $\gamma_{\mathrm{DW}} = 0.5\gamma$. The black asterisk indicates the nonlinear simulation belonging to the DW regime.

$k_\parallel = 0$, this reduction becomes small for $N \gg 1$ since $k_\parallel = m/(NR)$ is small. Moreover, for large N, the wave number $k_y \sim 2\pi l/L_v$ is substantially smaller for the resistive interchange mode ($l = 1$) than for the ideal interchange mode ($l = N$). With $k_y = 2\pi/L_v$ and $k_\parallel = 1/(NR)$, the stability condition of the resistive interchange mode due to $k_\parallel$ effects may be written as $\alpha_\parallel = 1$ with $\alpha_\parallel = [L_v c_s/(2\pi NR\rho_s)]^2/(2\gamma_I\hat{\nu})$. This condition is represented by the red lines in Fig. 4. The regions near and above the red curves correspond to $\alpha_\parallel \lesssim 1$ and are thus favorable for resistive interchange modes. Figure 3 reflects the typical character of this regime.

The third turbulence regime is dominated by DW. To study the importance of DW, we turn off the interchange drive: the curvature term in the vorticity Eq. (2). (We retain, however, the curvature-driven plasma compressibility terms mentioned earlier, which are stabilizing for both interchange and DW modes. At the small values of L_p/R that are most relevant for DW, however, these terms have only a small effect.) We again assume $\gamma \gg k_\parallel c_s$. We find DW are stable at weak gradients: $L_p/R \gtrsim 3/10$. Since the maximum DW growth rates scale as $\gamma \sim \omega_* \sim c_s/L_p$ for $k_\perp\rho_s \sim 1$, we expect them to dominate over interchange modes ($\gamma \sim c_s/\sqrt{RL_p}$) when $L_p/R \ll 1$. In this limit, the DW dispersion relation can be written as $\hat{\nu}k_y^2\rho_s^2\gamma^2 + k_\parallel^2 c_s^2(1 + 2.94k_y^2\rho_s^2)\gamma + (1 + 1.71\eta)ik_\parallel^2 c_s^2\omega_* = 0$. For resistive DW, $\nu > \gamma m_e/m_i$, the peak growth rate is $\gamma_{\mathrm{DW}}^{\max} \simeq 0.085(1 + 1.71\eta)c_s/L_n$, observed for $k_y\rho_s \simeq 0.57$, and $k_\parallel \simeq 0.24[\nu/(c_s L_p)]^{1/2}$, with a corresponding frequency of $\omega_{\mathrm{DW}}^{\max} \simeq 0.17(1 + 1.71\eta)c_s/L_p$. In the case of electron inertia-driven DW, $\nu < \gamma m_e/m_i$, the peak growth rate is $\gamma_{\mathrm{DW}}^{\max} \simeq 0.17c_s(1 + 1.71\eta)/L_n$ with a frequency $\omega_{\mathrm{DW}}^{\max} \simeq 0.25c_s(1 + 1.71\eta)/L_n$, observed for $k_y\rho_s \simeq 0.57$ and $k_\parallel \simeq (0.2/L_p)\sqrt{m_e/m_i}$. We identify the SMT DW regime by comparing the largest growth rate γ obtained from the full dispersion relation to γ_{DW}, the linear growth rate in the absence of the interchange drive (γ_{DW} is evaluated at the same l and n as the maximum γ). The regions to the left of the magenta curves in Fig. 4 correspond to $\gamma_{\mathrm{DW}} \gtrsim 0.5\gamma$, and are favorable for DW. The location of this curve may be estimated analytically with $\gamma_{\mathrm{DW}}^{\max} \gtrsim \gamma_I$, which leads to $L_{n,\mathrm{crit}}/R \simeq 0.013$ for $\nu > \gamma m_e/m_i$, and $L_{n,\mathrm{crit}}/R \simeq 0.05$ for $\nu < \gamma m_e/m_i$. In the simulations, we were able to produce DW dominated plasmas only at a value of the collisionality that is at least 1 order of magnitude lower than typical TORPEX experimental values. The nonlinear simulation belonging to the DW regime is indicated by the black asterisk in Fig. 4. At higher collisionalities, the interchange mode driven transport prevents the plasma gradients from ever steepening into the DW regime.

In contrast to TORPEX, the lower collisionality of typical Helimak argon discharges ($\nu = 0.0001c_s/R$, $L_v \sim 100\rho_s$, $L_n/R \sim 0.1$ [1]) leads to a substantially increased resistive interchange mode threshold, $N \sim 300$–400, that lies well above the $\alpha_\perp$ limit (typically $N \sim 25$–50). For N values between the two, as shown in the low ν and high L_v case of Fig. 4, the fastest growing instability predicted by our linear analysis is an electrostatic non-MHD drift-interchange mode with an adiabatic electron response and $\gamma \sim \gamma_I$ for $k_y\rho_s \sim 1$. The transport properties of this mode will be explored in future work.

In the parameter space explored here, the equilibrium sheared flows have at most a weak stabilizing effect on the turbulence. In Refs. [9,10], however, it was predicted, within the framework of two- and three-dimensional flux-tube simulations, that the strength of the sheared flows could be increased: (i) by increasing N or ν, or (ii) by increasing the strength of the sources. In the former case, the present simulations call into question the conclusions of the earlier works, since the resistive interchange mode was absent. In the case of stronger sources, our global simulations suggest that the strength of shear flow is sensitive to the boundary conditions at the upper and lower walls. More work is needed to reliably capture these boundary conditions.

We acknowledge many useful discussions with A. Fasoli, I. Furno, B. Labit, F. M. Poli, and C. Theiler.

*paolo.ricci@epfl.ch
†barrett.rogers@dartmouth.edu

[1] K. L. Wong *et al.*, Rev. Sci. Instrum. **53**, 409 (1982); E. D. Zimmerman and S. C. Luckhardt, J. Fusion Energy **12**, 289 (1993); P. K. Sharma and D. Bora, Plasma Phys. Controlled Fusion **37**, 1003 (1995); K. W. Gentle and H. Huang, Plasma Sci. Technol. **10**, 284 (2008); C. Riccardi *et al.*, Plasma Phys. Controlled Fusion **36**, 1791 (1994).
[2] A. Fasoli *et al.*, Phys. Plasmas **13**, 055902 (2006).
[3] F. J. Øynes *et al.*, Phys. Rev. Lett. **75**, 81 (1995); K. Rypdal and S. Ratynskaia, Phys. Rev. Lett. **94**, 225002 (2005).
[4] A. Loarte *et al.*, Nucl. Fusion **47**, S203 (2007).
[5] M. Shimada *et al.*, Nucl. Fusion **47**, S1 (2007).
[6] F. M. Poli *et al.*, Phys. Plasmas **13**, 102104 (2006); F. M. Poli *et al.*, Phys. Plasmas **15**, 032104 (2008).
[7] C. Riccardi *et al.*, Phys. Plasmas **4**, 3749 (1997); K. Rypdal and S. Ratynskaia, Phys. Plasmas **11**, 4623 (2004); J. C. Perez *et al.*, Phys. Plasmas **13**, 032101 (2006).
[8] B. LaBombard *et al.*, Nucl. Fusion **45**, 1658 (2005).
[9] P. Ricci and B. N. Rogers, Phys. Plasmas **16**, 092307 (2009).
[10] P. Ricci *et al.*, Phys. Rev. Lett. **100**, 225002 (2008).
[11] A. Zeiler *et al.*, Phys. Plasmas **4**, 2134 (1997).
[12] M. Podestà *et al.*, Plasma Phys. Controlled Fusion **48**, 1053 (2006).
[13] B. Li *et al.*, Phys. Plasmas **16**, 082510 (2009).